

Dust Masses in Three Other Supernova Remnants

5.1 Introduction

SN 1987A has provided a rare opportunity to follow the evolution of a CCSN in close detail and it is now well established that there is a significant mass of dust forming in the ejecta. However, the question of the dust budget problem in the early universe cannot be solved by considering SN 1987A alone. If CCSNe are indeed the primary source of the dust seen at high redshifts, it is necessary to establish that the majority of CCSNe do produce sizeable quantities of dust. This motivates the study of other CCSN remnants with the aim of determining the masses of dust that have formed in their ejecta.

Blue-shifted line emission is a common and long-lasting feature of the late-time spectra of CCSNe. In particular the emission lines of oxygen and hydrogen are often visible and often exhibit asymmetries and significant substructure (Milisavljevic et al. 2012). If these lines can be modelled then it may be possible to determine the dust masses in SNRs at late times (> 10 years).

There are only a few objects that lend themselves to this sort of modelling however. The primary obstacle to assessing a large number of late-time spectra from CCSNe is that the majority fade rapidly, with their brightness decreasing by eight magnitudes after maximum light within the first two years (Kirshner 1990). They are also frequently further

than ~ 10 Mpc from us and detections are relatively infrequent in the first place. As a result, the optical spectra are rarely visible after approximately 700 days (Milisavljevic et al. 2012).

However, there are a few unusual objects that, for various reasons, we may still be able to see many years or even decades after maximum light. This could be because they are unusually close, like SN 1987A, or more usually because some late-time energy source is illuminating the ejecta. The most obvious of these energy sources is the interaction between the forward shock and the surrounding circumstellar material. This interaction is known to stimulate emission across a wide range of wavelengths from radio to X-rays and causes a reverse shock to propagate inwards through the ejecta, heating and ionising the material it passes through. Other postulated energy sources include interaction between a central pulsar or magnetar and the expanding debris (Woosley 2010), or accretion onto a black hole (Patnaude et al. 2001).

Recent work by Milisavljevic et al. (2012) identified a number of CCSNe that were still visible in the optical despite being more than 20 years old. These included SN 1957D, SN 1970G, SN 1979C, SN 1980K, SN 1986E, SN 1986J, SN 1987A, SN 1993J and SN 1996cr. Many of these SNe exhibited strong asymmetries and blue-shifting in their profiles in the optical, particularly in the oxygen and hydrogen lines. In this chapter I present models of two of these objects for which Milisavljevic et al. (2012) presented new late-time optical spectra, namely SN 1980K and SN 1993J. I selected these since both exhibit a blue-shifted asymmetry in at least two line profiles in their late-time spectra and the lines of interest are largely uncontaminated by other lines. Unlike SN 1987A, in neither object has the forward shock encountered significant circumstellar material yet and thus the reverse shock has not started to propagate back through the ejecta allowing these late-time lines to be modelled.

In addition to these SNRs, I also present models of the oxygen lines of Cassiopeia A (Cas A). Cas A is a very well studied object. The combination of its age (it is ~ 300 years old) and nearby location has provided astronomers with an ideal opportunity to study supernova remnants at this epoch. I included Cas A in my modelling with the aim of understanding how the dust masses that form in the ejecta of CCSNe in the first few decades after outburst evolve over longer time frames.

By modelling asymmetries in the oxygen and hydrogen lines of these three objects, and by considering results from the line profile models of SN 1987A presented in the previous

chapter, I hope to start to paint a picture of dust formation in CCSNe; hopefully I will demonstrate that these objects do in fact seem to be capable of producing the quantities of dust that are necessary for them to provide the solution to the dust mass dilemma in the early universe.

5.2 SN 1980K and SN 1993J

SN 1980K is located in the Fireworks galaxy (NGC 6946) approximately 5.9 Mpc away (Karachentsev et al. 2000). It was discovered by P. Wild on 28 October 1980 and had reached a peak brightness of $V = 11.4$ mag by November that year (Buta 1982). The detection of the broad $H\alpha$ line in early spectra and a linearly decaying light curve after peak brightness resulted in its classification as a Type IIL supernovae (Barbon et al. 1982). SN 1980K continued to decline steadily in the optical although it was still detected almost seven years after maximum light by narrow passband imaging (Fesen & Becker 1988). Follow-up low dispersion observations found that the spectra exhibited broad $H\alpha$ and $[O\ I]\lambda\lambda 6300, 6363\ \text{\AA}$ emission with other weaker optical lines also present.

Spectroscopic and photometric observations of SN 1980K have revealed a very slow monotonic fading over a period of ~ 20 years. This unusually slow rate of decline suggested that the observations may in fact be a product of light echoes scattering off and heating circumstellar material as discussed in Section 1.1.8. This was first suggested for SN1980K by Chevalier (1986) based on early observations in the first year after outburst. Further modelling and analyses of late-time observations performed by Sugerman et al. (2012) found that light echoes were indeed present and that the evolution of the observations could be explained by scattered and thermal echoes off a thin circumstellar shell of dust of mass $\lesssim 0.02M_{\odot}$ approximately 14–15 lightyears from the progenitor. Of particularly relevance was their discussion of the origin of the high velocity $H\alpha$ and $[O\ I]\lambda\lambda 6300, 6363\ \text{\AA}$ lines which were not present in the early spectra during the first two years. They concluded that the shape of these lines could not be a product of a light echo since the high velocities seen in late-time spectra were not present in early spectra.

In 1981, the emergence of an IR flux excess provided the first indications of dust in the ejecta of SN 1980K (Dwek et al. 1983). However, it could not be confirmed whether

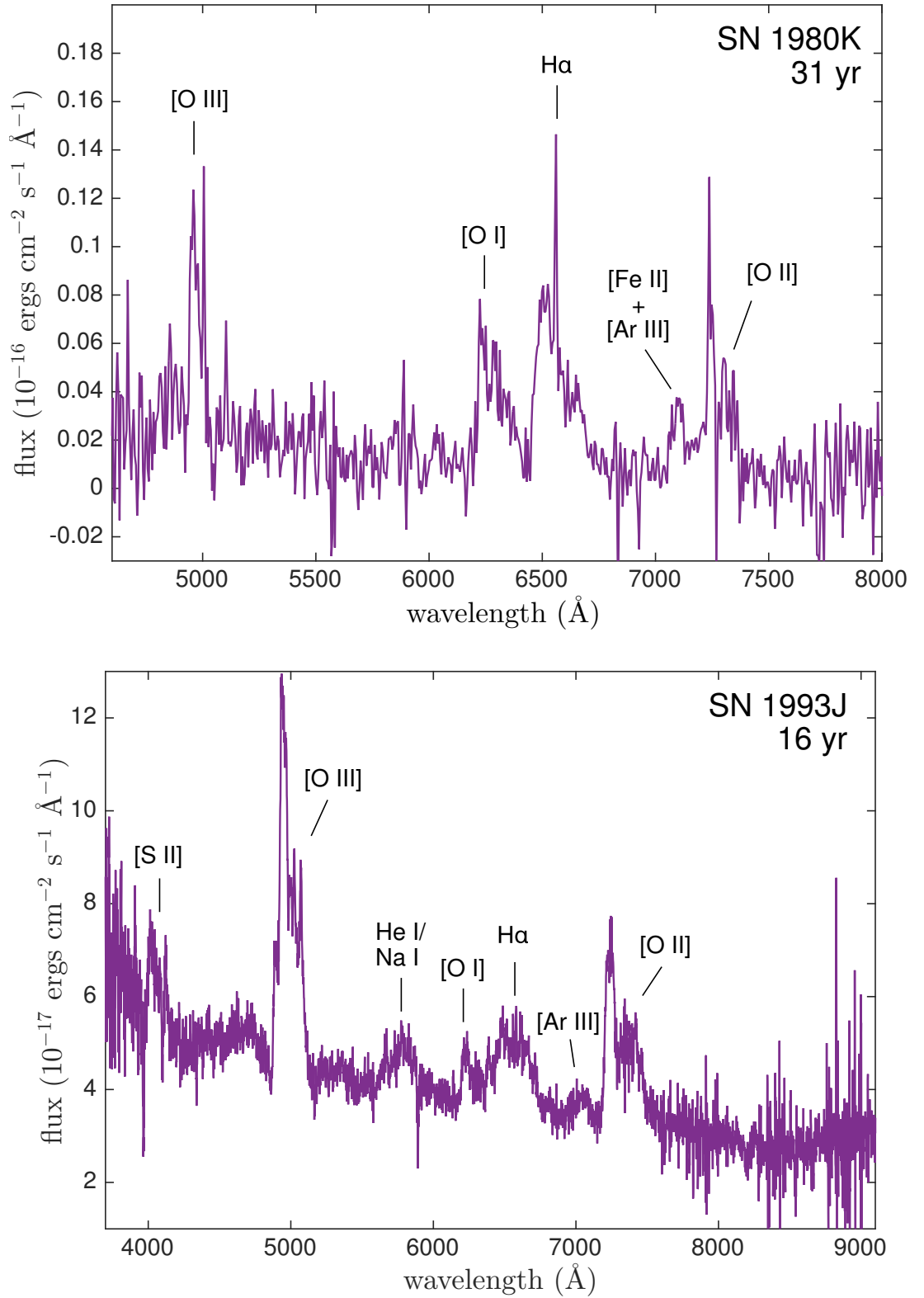


Figure 5.1. *Above:* The optical spectrum of SN 1980K on 9 October 2010 at 31 years post-explosion. *Below:* The optical spectrum of SN 1993J on 9 December 2009 at 16 years post-explosion. Both spectra were originally published by Milisavljevic et al. (2012).

this excess IR flux was the result of newly-formed dust condensing in the ejecta or from pre-existing grains located in a circumstellar shell and illuminated by radiation from the outburst. In addition to the detection of the signature emission from dust grains in the IR, highly blue-shifted line profiles in the optical spectra of SN 1980K have been observed for many years (Fesen & Becker 1990; Fesen & Matonick 1994; Fesen et al. 1995, 1999). The presence of dust in ejecta was postulated by Milisavljevic et al. (2012) based on the observed blue-shifting of these optical line profiles which are still present even in very late-time spectra (31 years). It is these latest blue-shifted line profiles of SN 1980K at 31 years that I have modelled and present here. An explosion date of 2 October 1980 is adopted for all models (Montes et al. 1998).

SN 1993J is a very well-observed and important supernova and is only surpassed by SN 1987A in regards to the quality and frequency of its observations. It is located in the nearby M81 galaxy 3.6 Mpc away (Freedman et al. 1994) and was discovered on 28 March 1993 (Ripero et al. 1993). It reached a maximum brightness of $V = 10.8$ mag making it the brightest supernova in the northern hemisphere since SN 1954A. It was swiftly classified as a Type II supernova due to early spectra exhibiting an almost featureless blue continuum. However, its evolution was atypical and the appearance of He lines in later spectra resulted in its classification as a Type IIb. The similarities to Type Ib and Type Ic supernovae were noted however and this supernova has been very important for understanding the relationship between the Type I and Type II categories (Filippenko et al. 1993; Garnavich & Ann 1993). Extensive reviews of SN 1993J are given by Wheeler & Filippenko (1996), who cover the early evolution of the object, and by Matheson et al. (2000a,b) who discuss the later evolution of the optical spectra.

SN 1993J is relatively isolated and quite close meaning that it has proved to be an ideal candidate for regular monitoring in the X-ray, radio and optical. I was particularly interested in late-time optical spectra obtained at 16 years post-outburst and the presence, or otherwise, of dust in the ejecta as postulated by Fransson et al. (2005) and (Milisavljevic et al. 2012). An explosion date of 27 March 1993 is adopted for all models (Baron et al. 1993).

5.2.1 The Late-Time Optical Spectra of SN 1980K and SN 1993J

Late-time spectra of both SN 1980K and SN 1993J were donated to me by Dr D. Milisavljevic. These spectra are published in Milisavljevic et al. (2012) and I present them here

in Figure 5.1.

Spectra of SN 1980K were obtained on 9 October 2010 using the 2.4m Hiltner telescope at the MDM observatory. The Mark III Spectrograph was used with a SITe 1024×1024 CCD detector and a $1.2'' \times 4.5'$ slit. Exposures were 2×3000 s and spectra spanned the wavelength range $4600 - 8000\text{\AA}$ with a spectral resolution of 7\AA . The spectrum presented in Figure 5.1 is of SN 1980K at approximately 31 years after outburst. Significant blue-shifting can be seen in virtually all lines, but especially in the $H\alpha$ and $[\text{O I}]\lambda\lambda 6300, 6363\text{\AA}$ lines which exhibit an pronounced flux bias towards the blue and a strongly blue-shifted peak.

The optical spectrum of SN 1993J was obtained on 9 December 2009 with the 6.5m Multiple Mirror Telescope (MMT) at Mt. Hopkins in Arizona using the HECTOSPEC optical fibre fed spectrograph. Spectra from the $1.5''$ diameter fibres covered the wavelength range of $3700 - 9200\text{\AA}$ with a full-width at half maximum (FWHM) resolution of 5\AA . The total exposure time was 3600s. The observations were obtained as a part of a survey of the supernova remnants in M81. SN 1993J was approximately 16 years old when the spectra were obtained. Many of the lines in the optical spectrum exhibit a flux-bias towards the blue and also display noticeable substructure. They are generally broad and there is a significant degree of blending between lines. The least blended lines are those of $[\text{O III}]\lambda\lambda 4959, 5007\text{\AA}$ and $[\text{O II}]\lambda\lambda 7319, 7330\text{\AA}$ which demonstrate a significantly asymmetrical profile, with both the flux and the peak of the profile shifted towards the blue.

Milisavljevic et al. (2012) reduced and calibrated the spectra of both objects by employing standard techniques in IRAF and their own routines, and removing any cosmic rays and obvious defects. For further details on the observations and calibrations of these spectra, please refer to Milisavljevic et al. (2012).

5.2.2 Line Profile Models of SN 1980K and SN 1993J

The modelling of SN 1980K focussed on the $H\alpha$ line and the $[\text{O I}]\lambda\lambda 6300, 6363\text{\AA}$ doublet. Both of these line profiles exhibited a very strong blue-shifted asymmetry indicative of the presence of dust in the ejecta and, like SN 1987A, were sufficiently distinct that they were the best options for modelling purposes. Other lines were either too blended with each other or too noisy to be reliable.

SN 1993J exhibited strongest asymmetries in the oxygen lines, and in particular I fo-

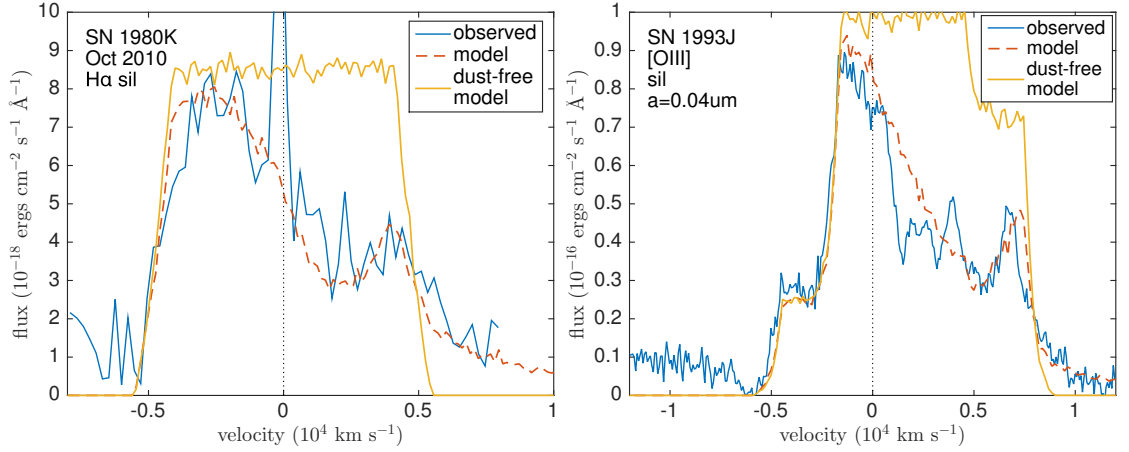


Figure 5.2. Best-fitting smooth models with the intrinsic dust-free boxy profile plotted for the $H\alpha$ line profile for SN 1980K (*left*) and the $[O\text{ III}]\lambda\lambda 5007,4959\text{ \AA}$ line profile for SN 1993J (*right*). The intrinsic dust-free modelled line profile is given in yellow, the dust-affected modelled line profile in red and the observed line profile in blue.

cussed modelling on the $[O\text{ II}]\lambda\lambda 7319,7330\text{ \AA}$ and $[O\text{ III}]\lambda\lambda 4959,5007\text{ \AA}$ doublets mentioned above. The $[O\text{ I}]\lambda\lambda 6300,6363\text{ \AA}$ doublet was not modelled for SN 1993J as it was quite blended with the $H\alpha$ line and the two lines could not be easily extricated. The $[O\text{ II}]$ and $[O\text{ III}]$ lines were more distinct and were therefore the more sensible candidates for modelling.

My approach to modelling the line profiles of both SN 1980K and SN 1993J followed the same principles as for SN 1987A that I detailed in Section 4.3. I began modelling by considering a smooth, coupled distribution of dust and gas before moving on to consider the effect on these models of including a clumped dust geometry whilst maintaining a smooth emissivity distribution. I first examined the line profile in order to determine the maximum and minimum velocities before moving on to establish approximately the exponent of the dust and gas density distribution. Having fixed the starting values for these quantities, I iterated over the grain size and dust mass in order to fit the profile. I also occasionally varied the other parameters in order to optimise the fit to the data. I assumed that the oxygen doublets were optically thin for both SN 1980K and SN 1993J and therefore adopted a constant intrinsic flux ratio of 3.1 between the $[O\text{ I}]\lambda\lambda 6300,6363\text{ \AA}$ components, 1.2 between the $[O\text{ II}]\lambda\lambda 7319,7330\text{ \AA}$ components and 2.9 between the $[O\text{ III}]\lambda\lambda 4959,5007\text{ \AA}$ components according to the theoretical flux ratios as detailed by Zeippen (1987) and Storey & Zeippen (2000). The intrinsic line profiles before dust effects

Table 5.1. The parameters used for the smooth and clumped models of SN 1980K for media composed of 100% amorphous carbon dust grains of radius $3.5\mu\text{m}$ or 100% silicate dust grains of radius $0.1\mu\text{m}$. Optical depths are given from R_{in} to R_{out} at $\lambda = 6300 \text{ \AA}$ for [O I] and $\lambda = 6563 \text{ \AA}$ for H α . The doublet ratio for the [O I] $\lambda\lambda 6300, 6363 \text{ \AA}$ was fixed to be 3.1. Smooth models are listed in the first four rows and clumped models in the last four rows.

	clumped?	species	a (μm)	V_{max} (km s^{-1})	V_{min} (km s^{-1})	R_{in}/R_{out}	β	M_{dust} (M_{\odot})	R_{out} (10^{17}cm)	R_{in} (10^{17}cm)	doublet	τ_{λ}	f	R_{clump} (10^{17}cm)
H α	no	sil	0.1	5500	4125	0.75	2.0	0.1	5.2	3.9	-	1.41	-	-
H α	no	amC	3.5	5500	4125	0.75	2.0	0.3	5.2	3.9	-	0.57	-	-
[O I]	no	sil	0.1	5500	4125	0.75	4.0	0.2	5.2	3.9	3.1	2.81	-	-
[O I]	no	amC	3.5	5500	4125	0.75	4.0	0.65	5.2	3.9	3.1	1.24	-	-
H α	yes	sil	0.1	5500	4125	0.75	2.0	0.12	5.2	3.9	-	1.68	0.1	0.2
H α	yes	amC	3.5	5500	4125	0.75	2.0	0.38	5.2	3.9	-	0.73	0.1	0.2
[O I]	yes	sil	0.1	5500	4125	0.75	4.0	0.3	5.2	3.9	3.1	2.81	0.1	0.2
[O I]	yes	amC	3.5	5500	4125	0.75	4.0	0.9	5.2	3.9	3.1	1.72	0.1	0.2

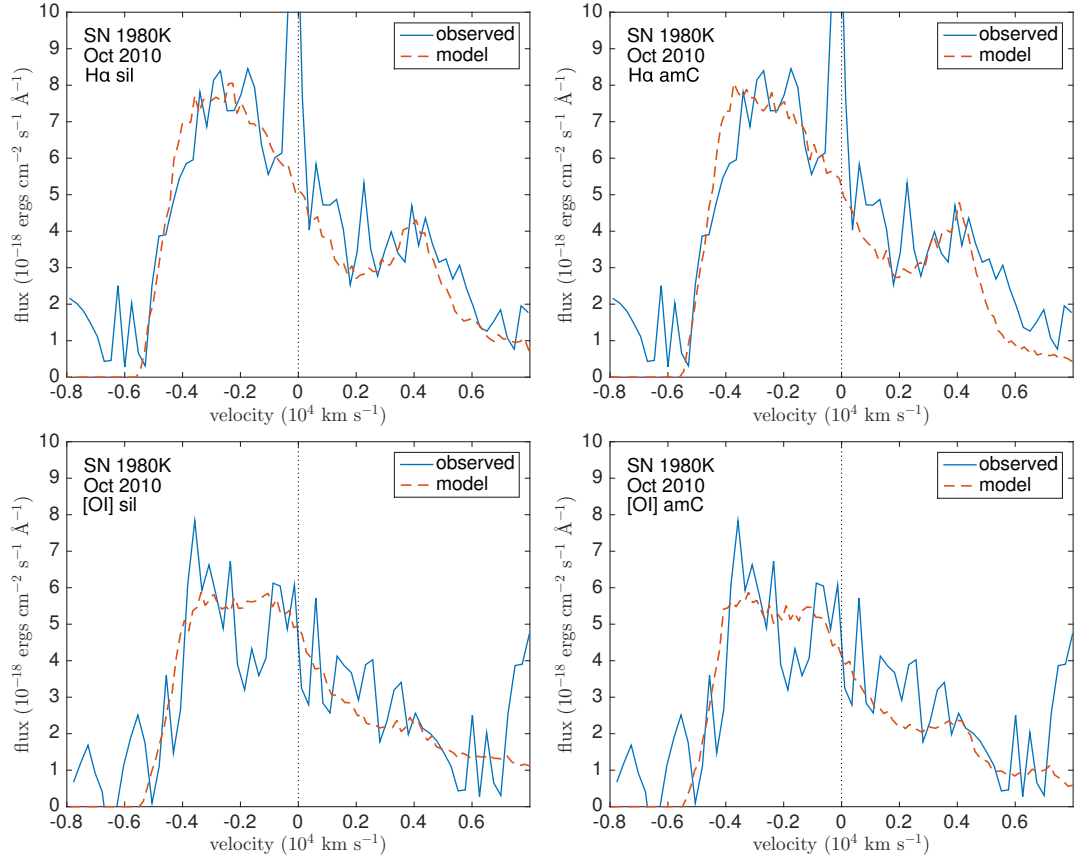


Figure 5.3. Best smooth dust fits to the SN 1980K H α (*top*) line and the [O I] $\lambda\lambda$ 6360,6363 Å doublet (*bottom*) for the parameters detailed in Table 5.1. Smooth dust fits with astronomical silicate grains of radius $a = 0.1\mu\text{m}$ are presented on the left and smooth dust fits with amorphous carbon grains of radius $a = 3.5\mu\text{m}$ are presented on the right.

for both SN 1980K and SN 1993J were both very ‘boxy’, that is, the ratio of the inner to outer radii was very high and the overall profile therefore has a very square shape. I present the intrinsic dust-free profile along with the best-fitting smooth H α model for SN 1980K in the left pane of Figure 5.2 and the intrinsic dust-free profile for the best-fitting smooth [O III] $\lambda\lambda$ 5007,4959 Å model for SN 1993J in the right pane of Figure 5.2.

The parameters for the smooth and clumped fits that I obtained for SN 1980K and SN 1993J are detailed in Tables 5.1 and 5.2 respectively. The smooth line profile fits for SN 1980K are presented in Figure 5.3 and the clumped line profile fits are presented in Figure 5.4. The smooth line profile fits for SN 1993J are presented in Figure 5.5 and the clumped line profile fits are presented in Figure 5.6.

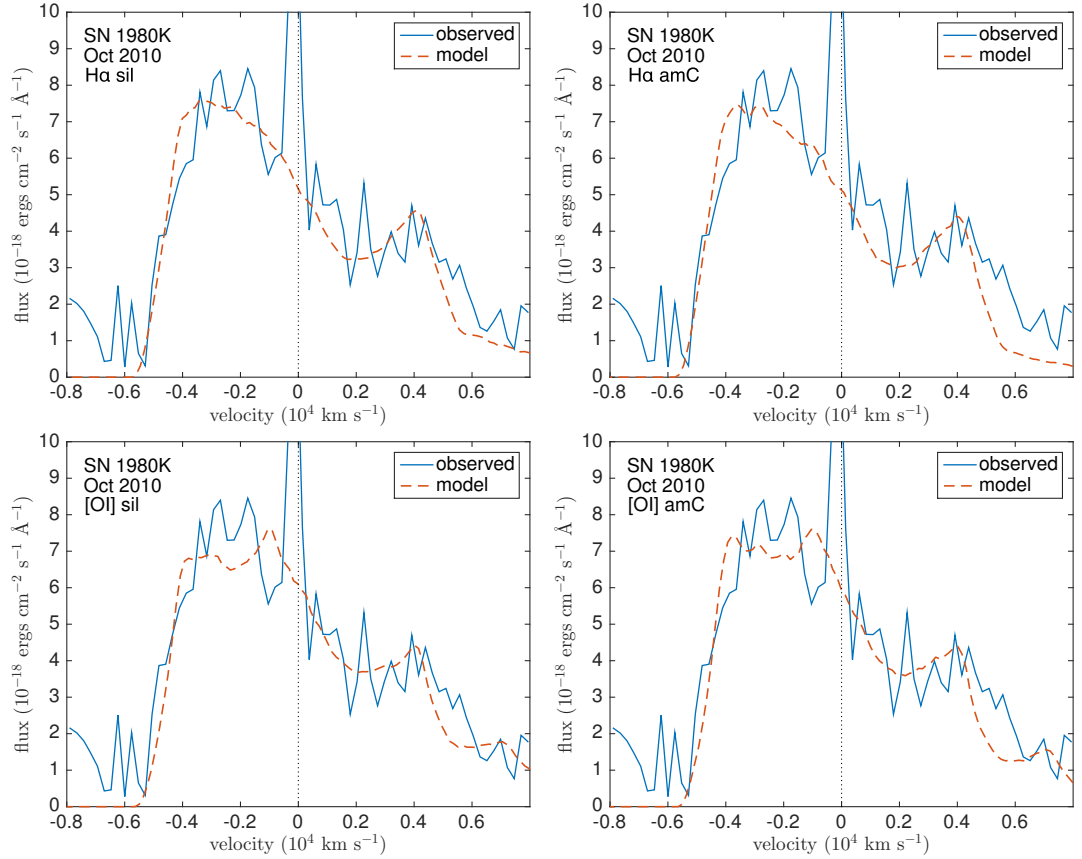


Figure 5.4. Best clumped dust fits to the SN 1980K H α line (*top*) and the [O I] $\lambda\lambda$ 6360,6363 Å doublet (*bottom*) for the parameters detailed in Table 5.1. Clumped dust fits with astronomical silicate grains of radius $a = 0.1\mu\text{m}$ are presented on the left and clumped dust fits with amorphous carbon grains of radius $a = 3.5\mu\text{m}$ are presented on the right.

Smooth Models of SN 1980K

I obtained good fits to both the H α and [O I] $\lambda\lambda$ 6300,6363 Å lines from SN 1980K (see Figure 5.3). In particular, an extended wing on the red side of the profile was seen in both cases. This was more important for the H α line since I could be sure that it was not a product of blending with an adjacent broad line (the presence of an extended red wing in the [O I] line may be due to blending with the blue wing of the H α line). This wing allowed me to place constraints on the albedo. A high albedo of $\omega \approx 0.8$ was required to reproduce the flux in the region between +6000 and +8000 km s $^{-1}$. Silicate grains of radius $a = 0.1\mu\text{m}$ have an albedo of this magnitude at this wavelength, but amorphous carbon grain are never this glassy regardless of their size. I include line profile fits using a large grain size ($a = 3.5\mu\text{m}$) for amorphous carbon to generate as high an albedo as possible ($\omega \approx 0.6$) illustrating the slightly worse, although still reasonably good, fit to the

Table 5.2. The parameters used for the smooth and clumped models of SN 1993J for media composed of 100% amorphous carbon dust grains of radius $3.5\mu\text{m}$ or 100% silicate dust grains of radius $0.1\mu\text{m}$. Optical depths are given from R_{in} to R_{out} at $\lambda = 7319 \text{ \AA}$ for [O II] and $\lambda = 4959 \text{ \AA}$ for [O III]. Smooth models are listed in the first four rows and clumped models in the last four rows.

	clumped?	species	a (μm)	V_{max} (km s^{-1})	V_{min} (km s^{-1})	R_{in}/R_{out}	β	M_{dust} (M_{\odot})	R_{out} (10^{17}cm)	R_{in} (10^{17}cm)	doublet	τ_{λ}	f	R_{clump} (10^{17}cm)
[O III]	no	sil	0.04	6000	4500	0.75	7	0.1	3.2	2.4	2.9	0.65	-	-
[O III]	no	amC	0.2	6000	4500	0.75	7	0.005	3.2	2.4	2.9	0.63	-	-
[O II]	no	sil	0.1	6000	4500	0.75	7	0.05	3.2	2.4	1.23	0.74	-	-
[O II]	no	amC	3.5	6000	4500	0.75	7	0.12	3.2	2.4	1.23	0.60	-	-
[O III]	yes	sil	0.04	6000	4500	0.75	7	0.15	3.2	2.4	2.9	1.00	0.1	0.13
[O III]	yes	amC	0.2	6000	4500	0.75	7	0.008	3.2	2.4	2.9	0.96	0.1	0.13
[O II]	yes	sil	0.1	6000	4500	0.75	7	0.08	3.2	2.4	1.23	1.12	0.1	0.13
[O II]	yes	amC	3.5	6000	4500	0.75	7	0.18	3.2	2.4	1.23	0.95	0.1	0.13

H α line, as well as the best-fitting silicates model in Figure 5.3.

Clumped Models of SN 1980K

Motivated by the modelling of SN 1987A, I adopted a clumped dust structure with a clump volume filling factor of $f = 0.1$ with clumps of width $R_{clump} = R_{out}/25$. All dust was located in clumps but the emission remained distributed smoothly according to the distribution derived for the smooth models. A summary of the parameters for the best-fitting clumped models is presented in Table 5.1 and the fits are presented in Figure 5.4.

Smooth Models of SN 1993J

I had mixed success in obtaining good fits to the oxygen line profiles of SN 1993J. Certain aspects of the line profiles are well-fitted by the models, such as the bump seen at -4000 km s^{-1} in the [O III] line. The peaks of the [O III] profile were fairly well matched although I could not reproduce the peak seen at $+4000 \text{ km s}^{-1}$. Similarly, I struggled to reproduce the shape of the profile between -2000 and $+2000 \text{ km s}^{-1}$ for both the [O III] and [O II] lines. In order to fit the profile, I needed to use different sized grains for the [O III] and the [O II] models in order to fit the red wing of the profile.

A manual investigation of parameter space suggested that these issues with fitting the shape of the profile derived from the initial emissivity distribution. The smooth nature of the emissivity distribution that I adopted could not reproduce the sharp downturn seen to the red side of the peak flux. I believe that this is likely due to an oxygen emission distribution that is potentially composed of a dense central region that produces the steep variations in the central regions with a more diffuse oxygen envelope accounting for the wings. A different geometry may well alter the effects of scattering and could therefore reduce or remove the discrepancy in the required grain sizes. I will discuss these issues in further detail in Section 5.2.3.

Parameters for the smooth models of [O III] $\lambda\lambda 4959, 5007 \text{ \AA}$ and [O II] $\lambda\lambda 7319, 7330 \text{ \AA}$ that are presented in Figure 5.5 are detailed in Table 5.2.

Clumped Models of SN 1993J

Clumped models of SN 1993J adopted the same clumped structure as for the SN 1980K clumped models and the SN 1987A clumped models ($f = 0.1$ and $R_{clump} = R_{out}/25$). All

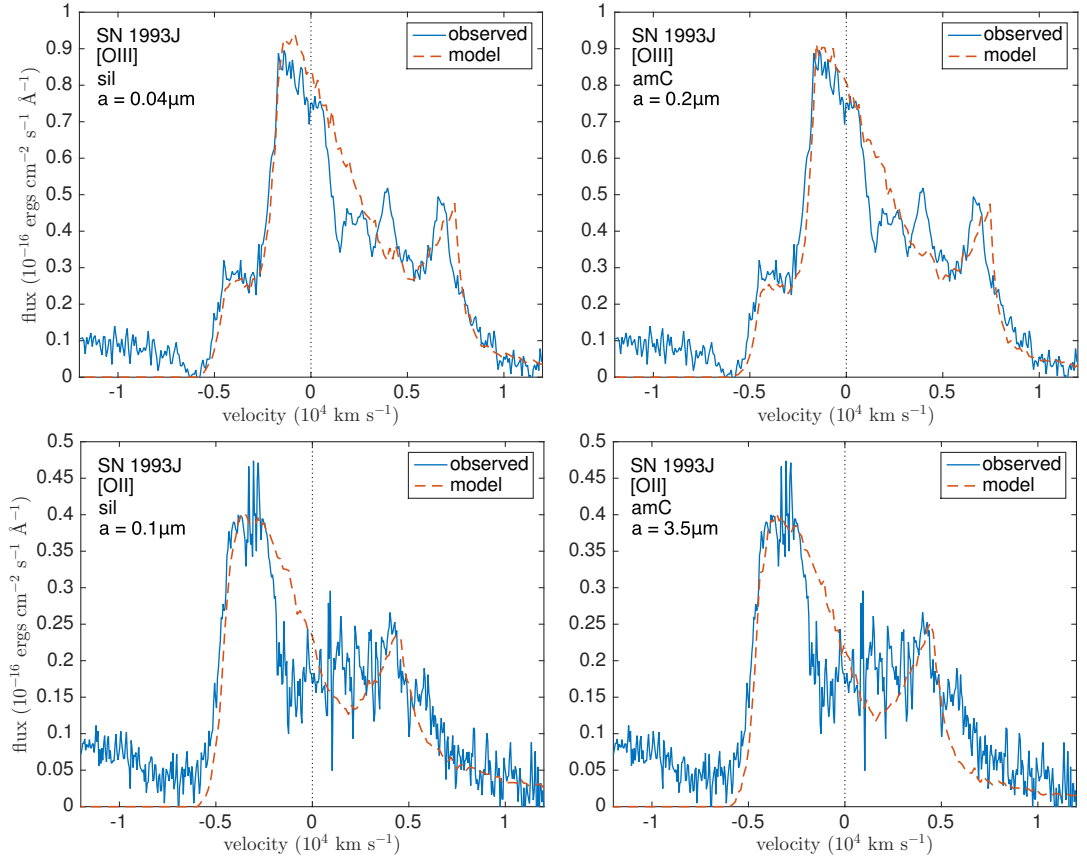


Figure 5.5. Best smooth dust fits to the SN 1993J [O III] $\lambda\lambda$ 4959,5007 \AA doublet (*top*) and the [O II] $\lambda\lambda$ 7319,7330 \AA doublet (*bottom*) for the parameters detailed in Table 5.2. Compositions and grain sizes are as detailed on the plots.

of the parameters were kept fixed from the smooth models except for the new clumped dust distribution. Similar fits were found and the clumped geometry had little effect on the resultant modelled line profiles. The required dust mass increased by a factor of approximately 1.5. The clumped models of [O III] $\lambda\lambda$ 4959,5007 \AA and [O II] $\lambda\lambda$ 7319,7330 \AA that are presented in Figure 5.6 are detailed in Table 5.2.

5.2.3 Discussion

SN 1980K

The models of the H α and [O I] $\lambda\lambda$ 6300,6363 \AA lines are broadly consistent with each other. The primary differences in the derived parameters are in the exponents of the density distributions and the total dust masses, with the oxygen distribution following a steeper trend than the more diffusely emitted hydrogen. In a similar manner to the early models of SN 1987A, the [O I] $\lambda\lambda$ 6300,6363 \AA line profile models require significantly

greater dust masses than the $H\alpha$ models. I believe that this is likely for the same reason that I discuss in Section 4.3.5, namely that dust forming regions are likely to include those which are oxygen rich (Kozma & Fransson 1998a). As a result, it seems possible that if the oxygen is located in clumps along with the dust then the discrepancy in the dust masses could potentially be resolved by considering more complex, decoupled distributions of dust and gas with diffuse hydrogen emission and clumped oxygen emission. I illustrated this possibility for SN 1987A in Chapter 4. I note that for clumped models the difference between dust masses derived from the $[O\ I]\lambda\lambda 6300, 6363\ \text{\AA}$ models and $H\alpha$ models is around a factor of approximately two, very similar to that seen for SN 1987A.

Both the $H\alpha$ and $[O\ I]$ line profiles exhibit an extended scattering wing which requires a glassy dust composition with a high albedo to fit it. Amorphous carbon models do not fit the red side of the $H\alpha$ profile very well, even for very large grain sizes and I therefore adopt the more reasonable silicate dust composition which fits the profiles slightly better. I note that a combination of species would also be capable of producing the high albedo necessary but would likely result in dust masses somewhere in between those of the amorphous carbon and silicate models. The poor signal-to-noise ratio of both profiles means that a small degree of variation in the parameters generates modelled line profiles that also fit the data reasonably. This is most important for the determination of the high albedo which is established based on a very small section of the observed line profile in the red wing of the data. Further observations with a higher signal-to-noise ratio would be beneficial for the purposes of line profile modelling.

There is limited discussion of the dust mass that may be present in the ejecta of SN 1980K other than its prophesied existence based on the asymmetrical line profiles that I fit here. The first suggestion of dust in the ejecta of SN 1980K was based on an IR flux excess seen a few hundred days after outburst (Dwek et al. 1983). Dwek et al. (1983) discussed the possibility of newly-formed dust in the ejecta accounting for this IR flux. However, they also acknowledged the possibility that the excess IR flux in the SED could also be a product of the reheating of pre-existing dust grains in the circumstellar material. Whilst this may in fact explain the early IR flux, dust in a circumstellar shell surrounding the supernova likely cannot explain the asymmetry observed in the optical line profiles. **As mentioned above, Sugerman et al. (2012) presented detailed modelling of the light echoes of SN 1980K. They concluded that thermal echoes off a thin circumstellar shell of dust of light emitted from a UV flash in the first two**

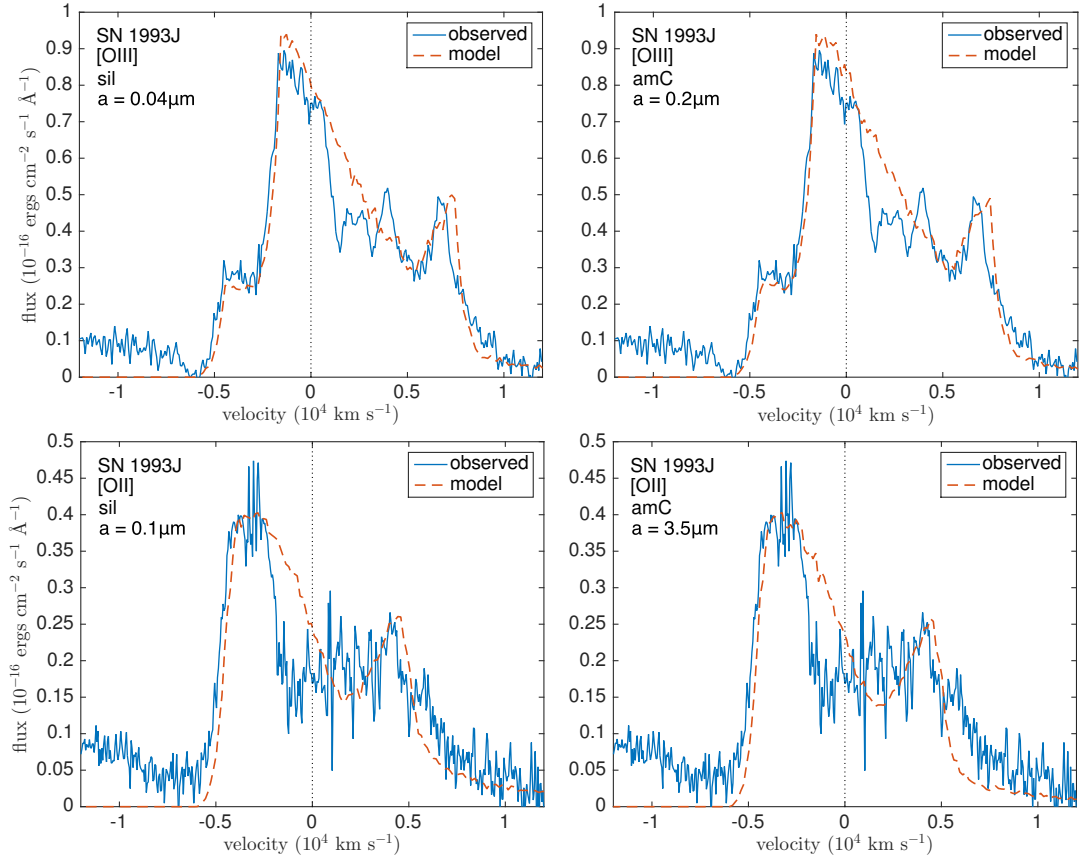


Figure 5.6. Best clumped dust fits to the SN 1993J [O III] $\lambda\lambda 4959, 5007 \text{ \AA}$ doublet (*top*) and the [O II] $\lambda\lambda 7319, 7330 \text{ \AA}$ doublet (*bottom*) for the parameters detailed in Table 5.2. Compositions and grain sizes are as detailed on the plots.

days, or of optical light emitted in the first 150 days, are contributing to the observed IR flux but that they can only account for a small fraction of it.

Other explanations for the stubborn presence of strongly blue-shifted asymmetrical optical lines have been discussed previously for SN 1980K with two primary explanations. Firstly, Fesen & Becker (1990) argue that broad asymmetrical lines in the early spectra arise as a result of the impact between the blast wave and pre-existing CSM. Similarly, Chugai & Danziger (1994) put forward a ‘clumpy wind’ model with emission coming from shocked clumps that could also explain the blue-shifted lines. Both of these mechanisms theoretically result in asymmetrical line profiles as a result of the stimulated emission from the approaching side of the supernova ejecta reaching us before emission from the receding side. However, both of these suggestions were ruled out based on analyses of the various time scales involved and their inability to reproduce the observed late-time excess IR flux by Sugerman et al. (2012). Fesen & Becker (1990) also noted the possibility of

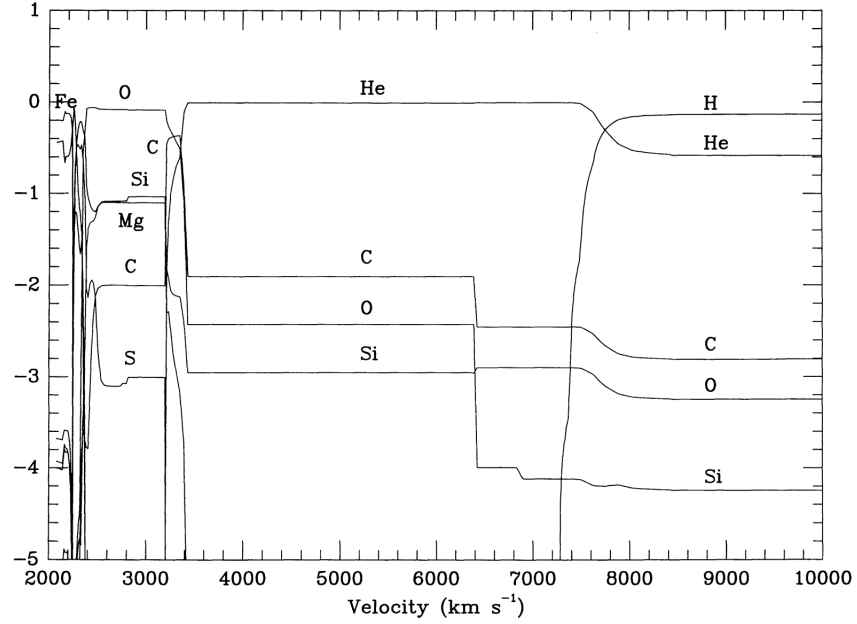


Figure 5.7. Composition of model 4H47 as a function of expansion velocity as computed by Nomoto et al. (1993).

blue-shifted lines arising as a result of dust forming in the ejecta but were doubtful as to the feasibility of the diffusely emitted hydrogen being so strongly affected by dust forming in the more dense, central regions of the ejecta. Sugerman et al. (2012) calculated that the ‘instantaneous’ dust mass needed to explain the MIR SED at similar epochs (23 – 30 years post-outburst) is $> 10^{-3} M_{\odot}$ with the presence of as much as a few M_{\odot} of cold dust possible. This latter possibility was noted based on the depth to which *Herschel* could probe during their FIR observations in 2010, i.e. a few M_{\odot} of cold dust could have been present in the ejecta of SN 1980K and still not been detected by *Herschel*. These results, though not particularly constraining, are consistent with my estimates of $0.1 - 0.9 M_{\odot}$.

SN 1993J

Models of the SN 1993J line profiles do not fit the observed data quite as well as the other models that I present in this thesis for other objects. In particular, the modelled profiles tend to over-estimate the flux in the region just to the red side of the peak flux where the observed profile exhibits a sharp downturn. The steepness of this drop cannot be matched by the models. However, certain other features of the observed profiles are fitted well by the model. For example, the $[\text{O III}]\lambda\lambda 4959, 5007 \text{ \AA}$ modelled line profile in particular fits bumpy features on both the red and blue sides of the profile at approximately

-4000 km s^{-1} and $+6000 \text{ km s}^{-1}$ quite well. The small discrepancy in the location of the peak at around $\sim 6500 \text{ km s}^{-1}$ is likely a result of a net velocity away from the observer (see Section 5.3.2 for a discussion of this effect in more detail) or a discrepancy between the smooth, symmetrical models and the likely more clumpy, asymmetrical geometrical structure of the remnant (Tran et al. 1997). Similarly, the difference in the grain size, and hence the dust mass, required to fit the [O III] and [O II] lines might also indicate the need for a different distribution of dust or gas. It is possible that the blue-shifted asymmetry in these lines is not a result of dust in the ejecta (the possibility of dust in the ejecta of SN 1993J has been noted only a few times), but it perhaps seems more likely, given how well certain aspects of the observed profiles are fitted, that it is simply the case that a more complex geometry is required for the models to better fit the data.

Houck & Fransson (1996) discuss the spectra of SN 1993J at somewhat earlier times than I consider here. The asymmetries that are present in the oxygen lines that I model here are also present at earlier times. Houck & Fransson (1996) suggest that this asymmetry can be explained by interaction between the lines. In particular, they discuss the effects of scattering by $\text{H}\alpha$ on the [O I] $\lambda\lambda 6300, 6363 \text{ \AA}$ line profile. It is possible that line blending effects the resultant profile, and it is logical that scattering by $\text{H}\alpha$ might cause the sharp drop in the line profile of [O I] that is seen on the red side. However, similarities in the late-time line profiles of [O I] $\lambda\lambda 6300, 6363 \text{ \AA}$ and [O II] $\lambda\lambda 7319, 7330 \text{ \AA}$ would suggest that the cause of this drop is more likely related to the geometrical structure of the emitting region rather than interaction with nearby lines.

Nomoto et al. (1993) produce a number of explosion models of a helium star as an analogue for a Type IIb supernova such as SN 1993J. From one of their models, they present a distribution of different elements throughout the expanding shell. As might be predicted from the line profiles, the oxygen is located in two distinct regions with significantly different densities (see Figure 5.7). The distribution of the oxygen in the models is smooth and it seems likely that the overestimation of the flux just to the red side of the peak could well be resolved by considering a two-component density distribution such as this.

It should also be noted that SN 1993J had a particularly unusual red supergiant progenitor with a stripped envelope caused by the presence of a B-star binary companion (Maund et al. 2004; Fox et al. 2014) and this system resulted in a significant mass of circumstellar material surrounding the supernova. Photometric analyses performed by

Zhang et al. (2004) suggest that the late-time optical emission from SN 1993J is largely powered by interaction between the blast wave and the circumstellar material. In this case, the geometry of the emitting regions is especially complex, and may in particular account for the significant substructure seen in the optical line profiles.

For both SN 1980K and SN 1993J, the effects of including a clumped dust distribution in the models rather than a smooth dust distribution serve to increase the required dust mass by a factor of approximately 1.5, very similar to that noted for SN 1987A from the models presented in the previous chapter. In these cases, the clumped geometry has little effect on the resulting profiles except to reduce the degree of absorption. The extent of the extended red scattering wing is also somewhat reduced.

5.3 Cassiopeia A

Cassiopeia A (Cas A) is a supernova remnant in the Cassiopeia constellation in the Milky Way and is a fairly unusual object in the night-sky. It is extremely close at only 3.4 kpc away and is rather large measuring around 3 pc in diameter (Reed et al. 1995). There have not been any records found of its detection around the time of its explosion. However, analysis of its expansion velocities and geometry have allowed its explosion date to be determined to be approximately 1681 ± 19 (Fesen et al. 2006b) making the supernova remnant approximately 330 years old. Cas A is the strongest radio source in the sky outside of the solar system and was initially observed at radio wavelengths in the 1940s. Since then, it has been well observed across the entire wavelength range. Recent observations in the NIR of light echoes caused by the reflection of early light from the supernova off surrounding circumstellar dust have allowed the original explosion to be probed. This work has suggested that Cas A is the result of a Type IIb supernova explosion with a progenitor stellar mass of $\sim 15M_{\odot}$ (Krause et al. 2008).

In Chapter 1, I discussed the importance of Cas A to our understanding of dust formation in supernovae and their remnants. Recent work on the mass and composition of dust in Cas A has suggested that the total dust mass present in the ejecta is of the order of $\sim 0.1M_{\odot}$ (Barlow et al. 2010; Nozawa et al. 2010; Arendt et al. 2014). Previous estimates, however, are significantly more wide-ranging from less than $3 \times 10^{-3}M_{\odot}$ to greater than $4M_{\odot}$ (Milisavljevic et al. 2012).

A late-time spectrum of Cas A reveals that asymmetries in line profiles in the optical are

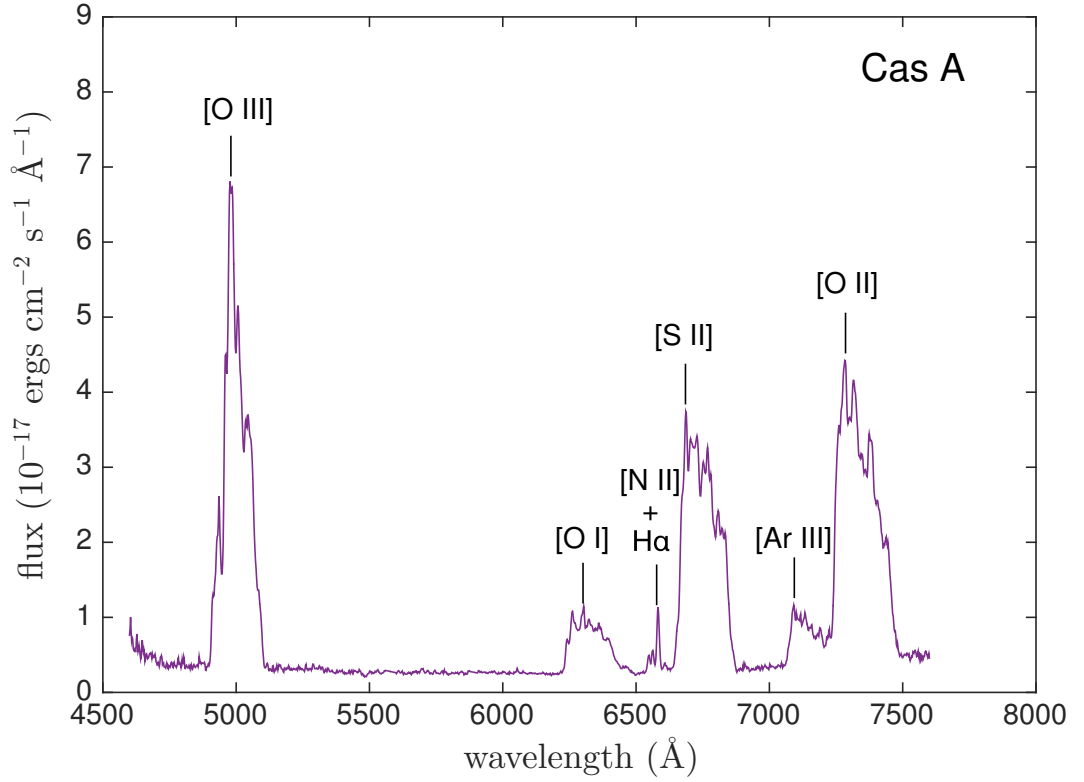


Figure 5.8. The integrated spectrum of Cas A (Milisavljevic & Fesen 2013).

still visible. In particular, the oxygen lines $[\text{O I}]\lambda\lambda 6300, 6363 \text{ \AA}$, $[\text{O II}]\lambda\lambda 7319, 7330 \text{ \AA}$ and $[\text{O III}]\lambda\lambda 4959, 5007 \text{ \AA}$ still exhibit a blue-shifted asymmetry, with the $[\text{O III}]$ line especially demonstrating a strong blueshift with considerable substructure. I have modelled all three of these lines with a primary focus on the $[\text{O III}]$ doublet.

5.3.1 The Integrated Spectrum

The integrated spectrum of Cas A presented in Figure 5.8 is from Milisavljevic & Fesen (2013) and was kindly provided to me by Dr D. Milisavljevic. It is composed of observations from a series of observing runs between September 2007 and November 2010 that were conducted in order to obtain low-dispersion optical spectra across the remnant. The majority of observations were carried out at the MDM Observatory at Kitt Peak, Arizona using the 2.4m Hiltner telescope and the Mayall 4m telescope. The MDM Modular Spectrograph was used with an ‘Echelle’ detector. A long slit of dimensions $2'' \times 5'$ was used and was oriented North-South. Exposure times were generally $2 \times 500\text{s}$. The wavelength range covered was $4500\text{--}7000 \text{ \AA}$ with a spectral resolution of 6 \AA . The integrated spectrum

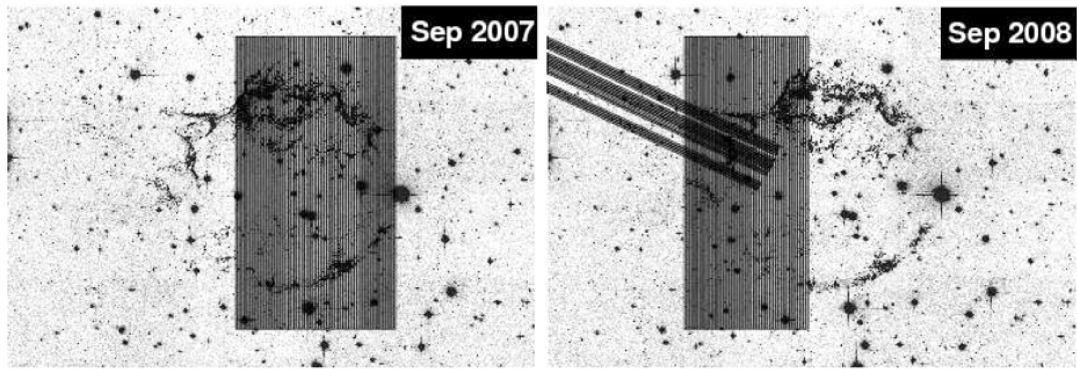


Figure 5.9. Finding charts of the long-slit positions used to compose the integrated spectrum of the main shell of Cas A. The background image is a mosaic created from 2004 HST/ACS observations (Fesen et al. 2006a). Image is taken from Milisavljevic & Fesen (2013).

was ultimately composed of 80 long slit spectra spaced $3''$ apart across the entire main shell which is approximately $4'$ in diameter. The slit positions are shown in Figure 5.9. Assuming an explosion date of 1681, this spectrum of Cas A is approximately 325 years old.

5.3.2 Smooth Models of the Oxygen Lines

The modelling of the Cas A spectrum was initially focussed on the $[\text{O III}]\lambda\lambda 4959, 5007 \text{ \AA}$ line, which exhibits a pronounced asymmetry. The process of finding a fit to the line profile was the same as described in Sections 4.3 and 5.2.2, i.e. the maximum velocity was identified from the point at which flux vanishes on the blue side, the inner to outer radius ratio determined from various inflection points and the density profile determined from the shape of the profile. The other parameters were then iterated over to find the best fitting profile.

I managed to produce a reasonable fit to the data using the parameters listed in the first row of Table 5.3. The profile is presented in the left pane of Figure 5.11. As can be seen, the modelled line profile generally fits the observed line profile quite well, although it fails to fit the red side of the profile adequately. A thorough, manual investigation of parameter space resulted in the conclusion that the profile was much better fitted if the entire observed profile was shifted to the blue by -700 km s^{-1} . This might well be a reasonable assumption. Cas A is known to be significantly asymmetrical (Rest et al. 2011) with radial velocities spanning -4000 to $+6000 \text{ km s}^{-1}$ (Milisavljevic & Fesen 2013)

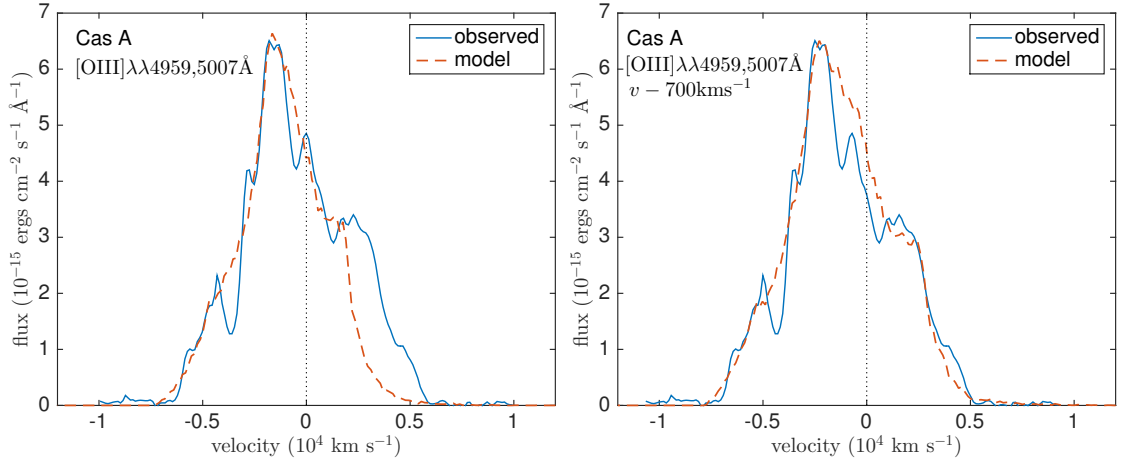


Figure 5.10. Best smooth dust fits to the Cas A [O III] $\lambda\lambda 4959, 5007 \text{ \AA}$ doublet for the parameters detailed in Table 5.3. On the left is the original [O III] line profile and on the right the observed [O III] line has been shifted uniformly towards the blue by -700 km s^{-1} .

suggesting that the net line-of-sight velocity is likely away from the observer and indicating the need for an overall velocity shift to correct for this. I found that models of the [O II] $\lambda\lambda 7319, 7330 \text{ \AA}$ and [O I] $\lambda\lambda 6300, 6363 \text{ \AA}$ lines were also substantially improved if the entire profile was allowed to be uniformly shifted towards the blue. For the remainder of the models I therefore shifted the profiles in velocity space to better fit the data based on the likelihood that the sampled emitting regions had an overall net velocity away from the observer. Fits to the line profiles were significantly improved following this translation (see Figures 5.11 to 5.12).

A model of the shifted [O III] $\lambda\lambda 4959, 5007 \text{ \AA}$ line is presented in Figure 5.11 and the parameters used for this model are presented in the second row of Table 5.3. The line profile was shifted by -700 km s^{-1} . A total dust optical depth of $\tau = 0.49$ at 5007 \AA between R_{in} and R_{out} was found to best fit the profile. An albedo of $\omega \approx 0.15$ at 5007 \AA was also necessary.

The composition of the dust has a significant effect on the overall dust mass for this optical depth and albedo. A line profile model of the [O III] line profile from Cas A could not be found using 100% astronomical silicate dust (Draine & Lee 1984). There is little to no scattering wing seen, hence the relatively low value of ω , and therefore relatively small silicate grains would be required to reproduce the red side of the profile. Silicate grains of this size have extremely low absorption efficiencies and therefore the best-fitting optical depth of $\tau = 0.49$ corresponds to an implausibly large mass of dust ($> 20 M_{\odot}$) if it

Table 5.3. The parameters used for the smooth models of Cas A with a medium composed of 50% amorphous carbon and 50% silicate grains of radius $a = 0.05 \mu\text{m}$. Optical depths are given from R_{in} to R_{out} at $\lambda = 5007 \text{ \AA}$ for [O III], $\lambda = 7319 \text{ \AA}$ for [O II] and $\lambda = 6300 \text{ \AA}$ for [O I]. The doublet ratio is always the ratio of the stronger line to the weaker line. The asterisk indicates that the parameters listed describe the gas density distribution. The dust density distribution is the same in all cases (as detailed for the shifted [O II] doublet in the second row).

	v shift (km s^{-1})	V_{max} (km s^{-1})	V_{min} (km s^{-1})	R_{in}/R_{out}	β	M_{dust} (M_{\odot})	R_{out} (10^{18}cm)	R_{in} (10^{18}cm)	doublet ratio	τ_{λ}
[O III]	0	4500	1800	0.4	2.0	0.9	4.7	1.9	2.9	0.53
[O III]	-700	5000	2500	0.5	2.0	1.1	5.2	2.6	2.9	0.49
[O II]*	-1000	5000	3250	0.65	2.0	1.1	5.2	3.4	1.23	0.21
[O I]*	-1000	5000	3250	0.65	2.0	1.1	5.2	3.4	3.1	0.30

is composed entirely of astronomical silicates.

The chemical composition of the dust in the ejecta of Cas A is known to be extremely complex (Arendt et al. 2014) with many different species of dust grain present in the ejecta. The presence of silicate dust has been predicted based on typical silicate emission features observed in the IR region of the spectrum. However, the presence of a variety of other species is also predicted. I therefore investigated the dust masses required to fit the profile for varying fractions of silicate and amorphous carbon dust. In Table 5.4, I detail the dust masses required to fit the [O III] $\lambda\lambda 4959, 5007$ Å line profile for different fractions of silicates and amorphous carbon grains for a single grain size. For each composition I determine the grain radius based on the albedo necessary to fit the profile ($\omega \approx 0.15$) and then vary the dust mass to achieve the required optical depth. The calculated dust masses cover a wide range of values between $0.37 - 6.5M_{\odot}$.

It might have been possible to approximately determine the composition based on the relative optical depths necessary to fit different blue-shifted lines in the spectrum and the wavelength dependence of dust absorption for different compositions. I therefore considered fitting the blue-shifted [O II] $\lambda\lambda 7319, 7330$ Å and [O I] $\lambda\lambda 6300, 6363$ Å lines from Cas A. Sadly, at the small grain sizes required, there is not significant variation in the relationship between the absorption efficiencies at 5007Å and 7319Å for different dust compositions and I cannot therefore determine the composition via this approach in this case. Additionally, the [O II] and [O I] lines are much less sensitive to variations in both distribution and dust mass, partly due to the high frequency of bumpy features observed in these lines which contaminate the intrinsic broad profile. The best-fitting models for these lines were therefore quite degenerate i.e. there were multiple sets of parameters that resulted in reasonable fits.

However, it was possible to use these lines to determine the feasibility of the best-fitting model of the [O III] $\lambda\lambda 4959, 5007$ Å line profile. I adopted the dust distribution that I determined using the [O III] line and investigated models for the [O II] $\lambda\lambda 7319, 7300$ Å and [O I] $\lambda\lambda 6300, 6363$ Å line profiles to see if this dust distribution were capable of fitting these lines as well. I adopted an emissivity distribution that was slightly different to the [O III] line (see Table 5.3) and shifted the observed line profiles by -1000 km s^{-1} . These emissivity distributions were modelled with the dust distribution and dust mass for the best-fitting smooth [O III] model. The resultant [O II] and [O I] line profiles are very good fits (see Figure 5.10). This suggests that the models are consistent and, if the relative

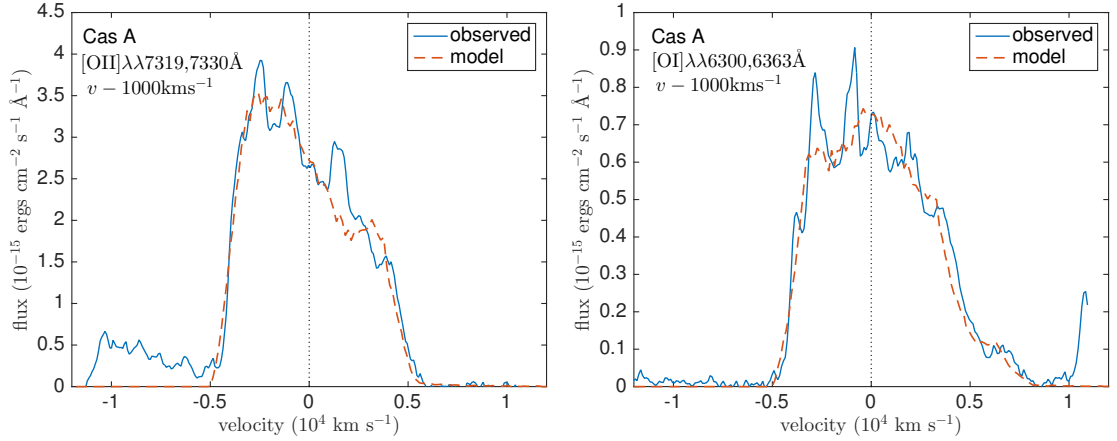


Figure 5.11. Best smooth dust fits to the Cas A [O II] $\lambda\lambda 7319,7330$ Å doublet (*left*) and the [O I] $\lambda\lambda 6300,6363$ Å doublet (*right*) for the parameters detailed in Table 5.3. Both observed line profiles have been shifted uniformly towards the blue by -1000 km s^{-1} .

abundance of species can be determined via other means, that the dust mass can be well-constrained using this method. All of the line profile models listed above adopted intrinsic doublet strengths from the theory as detailed by Zeppen (1987) and Storey & Zeppen (2000).

5.3.3 Clumped Models of the Oxygen Lines

The ejecta of Cas A is highly clumped. Recently, models by Biscaro & Cherchneff (2014) have suggested that dust cannot in fact form in the gas phase in the ejecta of Cas A unless extremely dense knots of material are present. It is therefore important, as with SN 1987A, to consider the effects of clumping on the line profiles. I continue to focus on the [O III] line profile from Cas A and consider the effects of clumping. Clearly, the ejecta has a complex geometry with many clumps of different sizes and likely different ionisation states and dust species within each. The models that I present here are included to give some indication of the effects of clumping within the ejecta rather than to be representative of the state of the ejecta at this time. To this end I present a number of models of the [O III] line profile based on the smooth fits that I presented in the previous section. I consider two different clump sizes, ones with width $R_{out}/25$ and ones with width $R_{out}/10$. I also consider three different clump volume filling factors $f = 0.05$, $f = 0.1$ and $f = 0.25$. For each combination of clump size and filling factor I evaluate the required increase or decrease in the dust mass over the smooth model. All other parameters were kept fixed such that packets were

Table 5.4. The variation in dust mass for a fixed optical depth $\tau_{5007\text{\AA}} = 0.49$ for the parameters listed in Table 5.3.

% silicate grains	% amorphous carbon grains	grain radius a (μm)	M_{dust} (M_{\odot})
90	10	0.035	6.5
75	25	0.04	2.5
50	50	0.045	1.1
25	75	0.048	0.6
0	100	0.05	0.37

emitted according to the smooth distribution and geometry described by the parameters listed in Table 5.3.

The change in the required dust mass is listed as a fraction of the smooth dust mass (e.g. $M_{dust} = 1.1M_{\odot}$ for a medium of 50% astronomical silicates and 50% amorphous carbon – see Table 5.4 for other dust masses with different dust compositions) is given in Table 5.5. Whilst clumping serves to increase the required dust mass in all cases, in the most extreme it is still only by a factor of ~ 3.5 . The fits for all of these cases are presented in Figure 5.12.

5.3.4 Discussion

The models of Cas A adopt a maximum expansion velocity of $\sim 5000 \text{ km s}^{-1}$ which gives an outer radius of $5.2 \times 10^{18} \text{ cm}$ equivalent to a diameter of 3.5 pc . These values are broadly consistent with an angular diameter of approximately $4' \approx 4 \text{ pc}$ (Hurford & Fesen 1996) and radial velocities between -4000 km s^{-1} and $+6000 \text{ km s}^{-1}$ (DeLaney et al. 2010). In particular, the need to shift the profiles by -700 km s^{-1} or -1000 km s^{-1} in order to fit them is consistent with the expansion velocity asymmetry observed by DeLaney et al. (2010); an offset of 1000 km s^{-1} applied to an originally symmetrical distribution between -5000 km s^{-1} and $+5000 \text{ km s}^{-1}$ results exactly in the velocity range that they predicted. DeLaney et al. (2010) predict an average velocity offset away from the observer of 859 km s^{-1} , almost exactly halfway between the 700 km s^{-1} and 1000 km s^{-1} velocity offsets that I adopt for the [O III] line and the [O I] and [O II] lines respectively. The difference in these values is likely a result of different ionisation fractions at different points in the nebula.

In general, the structure of the Cas A remnant is a lot more complex than the simple shell geometry adopted here. Cas A can be assumed to be composed of a spherical

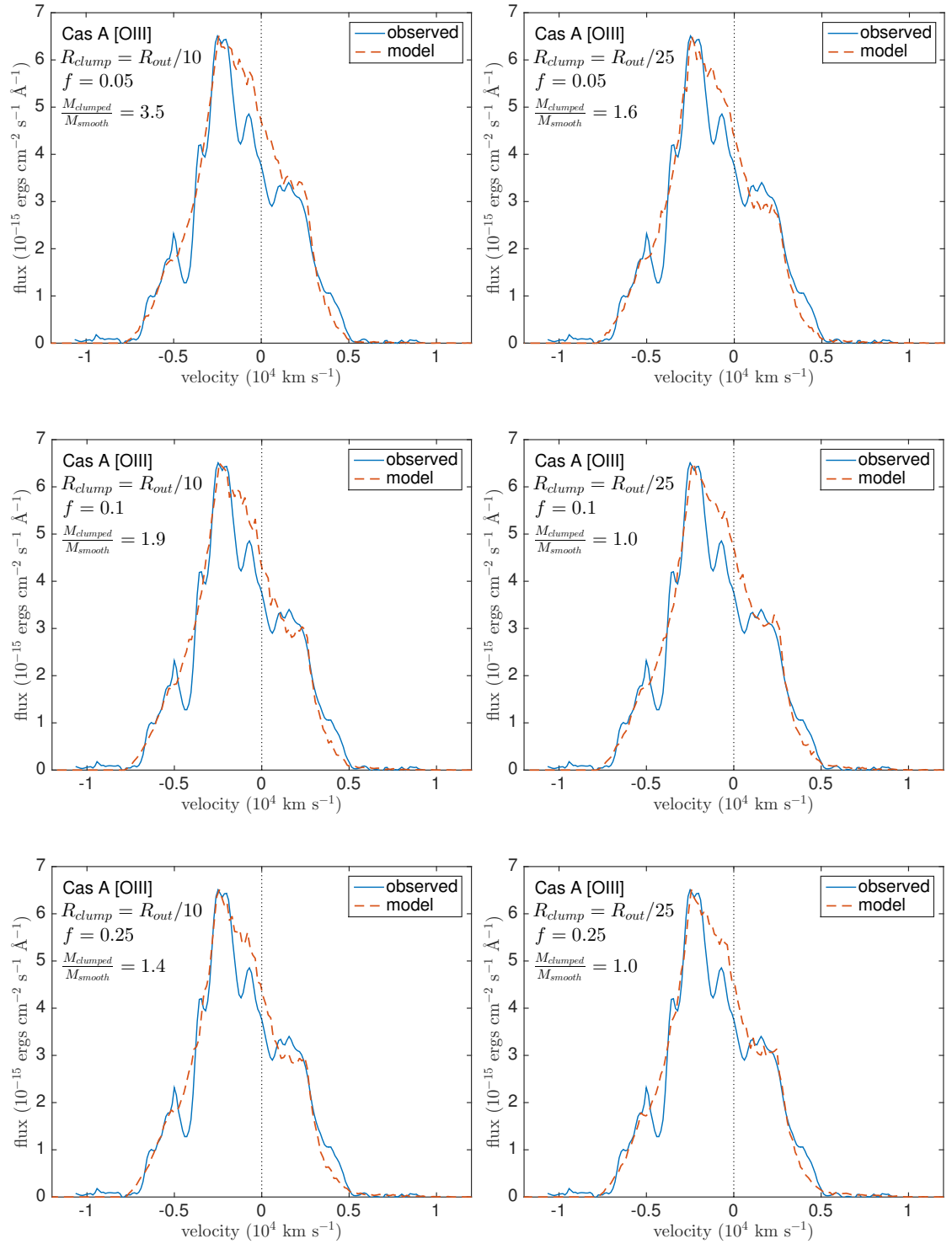


Figure 5.12. Best clumped dust fits to the Cas A [O III] $\lambda\lambda 4959, 5007$ Å doublet for the parameters described in Tables 5.3 and 5.5. In the left column are fits to the profile using a clumps of width $R_{\text{clump}} = R_{\text{out}}/10$ and in the right column are fits using clumps of width $R_{\text{clump}} = R_{\text{out}}/25$. Each row uses a model that adopts a different clump volume filling factor with $f = 0.05$ on the top, $f = 0.1$ in the middle and $f = 0.25$ on the bottom. The observed profile has been shifted uniformly towards the blue by -700 km s^{-1} .

Table 5.5. The fraction of increase in dust mass over the smooth model with parameters as given in Table 5.3 for clumped models with different clump widths and different clump volume filling factors. The other parameters in the models were fixed at the values given in Table 5.3.

	$f = 0.05$	$f = 0.1$	$f = 0.25$
$R_{out}/10$	3.5	1.9	1.4
$R_{out}/25$	1.6	1.0	1.0

component, a tilted thick disk, and multiple ejecta jets and optical fast-moving knots all populating the thick disk plane (DeLaney et al. 2010). These knots are the cause of some of the noticeable bumpy substructure of the emission lines that I model here. The models that I have presented above represent a first-order approximation to the geometry of Cas A and future work will hopefully include a more realistic density distribution.

It is not just the geometrical structure of the Cas A remnant that is complex. The chemical composition of the nebula is also extremely varied and there is evidence for numerous different dust species including silicates, silicon carbide (SiC), alumina (Al_2O_3) and carbonaceous grains (Arendt et al. 2014; Biscaro & Cherchneff 2014). These species also appear to be located in different clumps or regions of the ejecta. It has even been suggested that the dust could be composed of iron needles which produce a distinctly different SED to more commonly considered grains (Dwek 2004). Iron grains have a similar absorption efficiency to amorphous carbon grains for a given cross-sectional area but are about three times denser. Arendt et al. (2014) conclude that the entire spectrum of Cas A can be fitted using only four dust species: $\text{Mg}_{0.7}\text{SiO}_{2.7}$, $\text{Mg}_{2.4}\text{SiO}_{4.4}$, Al_2O_3 and amorphous carbon. Two of these species are highly scattering and two are relatively absorbing. This might suggest that one of the dust composition models with both silicates and amorphous carbon is likely the most representative. However, whilst there is evidence for a variety of species in the warm dust component, the cool component that has not yet been heated by the passage of the reverse shock and constitutes the majority of the dust in the ejecta is still of unknown composition (Arendt et al. 2014) and so constraining the dust mass is difficult.

Given the difficulties in modelling this object, it is perhaps not surprising that there is significant variation in the estimates of the dust mass in the ejecta. Barlow et al. (2010) present a brief review of the ejecta dust mass estimates in Cas A up to 2010. Early dust mass estimates were largely based on observations of the warm dust component in

the ejecta. Arendt et al. (1999) estimated a mass of $0.038M_{\odot}$ of 52 K dust based on fitting IRAS $60\mu\text{m}$ and $100\mu\text{m}$ fluxes. A similar mass of $0.020 - 0.054M_{\odot}$ of warm dust at $65 - 265\text{K}$ was estimated to be emitting between $5\mu\text{m}$ and $70\mu\text{m}$ by Rho et al. (2008), particularly in a bright ring associated with the reverse shock. Observations at longer wavelengths of the cold dust in the ejecta have predicted higher masses with Dunne et al. (2003) using SCUBA data to place the dust mass at between $2 - 4M_{\odot}$. This was contested by Krause et al. (2004) who suggested that the majority of this emission could be from cold dusty clouds located along the line of sight to Cas A. They placed an upper limit of $0.2M_{\odot}$ of cold dust in the ejecta. However, observations of strongly polarised emission at long wavelengths obtained using the SCUBA polarimeter have been used to argue an ejecta-condensed cold dust mass of $\sim 1M_{\odot}$ (Dunne et al. 2009). Modelling by Nozawa et al. (2010) reproduced the observed IR SED using $0.08M_{\odot}$ of which $0.072M_{\odot}$ remained inside the reverse shock. They could not isolate a cold dust component to be within the ejecta but estimated its mass to be $\sim 0.06M_{\odot}$. Further observations by Barlow et al. (2010) using *Herschel* estimated a cold dust component associated with the remnant of $0.075 \pm 0.028M_{\odot}$ of silicate dust. Finally, Arendt et al. (2014) used *Spitzer* observations to derive a mass of $\sim 0.04M_{\odot}$ of warm dust and limited the cool component in the unshocked ejecta to $< 0.1M_{\odot}$.

Even accounting for the adoption of different species, the dust masses given by the models are generally somewhat higher than these more recent estimates. However, they are broadly consistent with those estimates by Dunne et al. (2003) and Dunne et al. (2009). Whilst it seems that there is general agreement over the mass of the warm dust component, there is still disagreement regarding the mass of cool dust in the ejecta. This is particularly difficult to establish for Cas A from photometric observations and SED fitting because of the presence of interstellar clouds of cool dust along the line-of-sight that contribute to the observed fluxes at long wavelengths. Disentangling the relative flux contributions from Cas A and the interstellar clouds is not straightforward.

Based on SN 1987A, one might expect the cool dust component to be significantly larger than that of the warm dust component. However, the two supernovae are of different types. Biscaro & Cherchneff (2014) point out that the diffuse nature of Type IIb supernovae compared to their Type IIP counterparts is such that they struggle to form the molecules and molecular clusters that go on to form dust grains.

Cas A is the only object to have had the mass of dust in its ejecta predicted quanti-

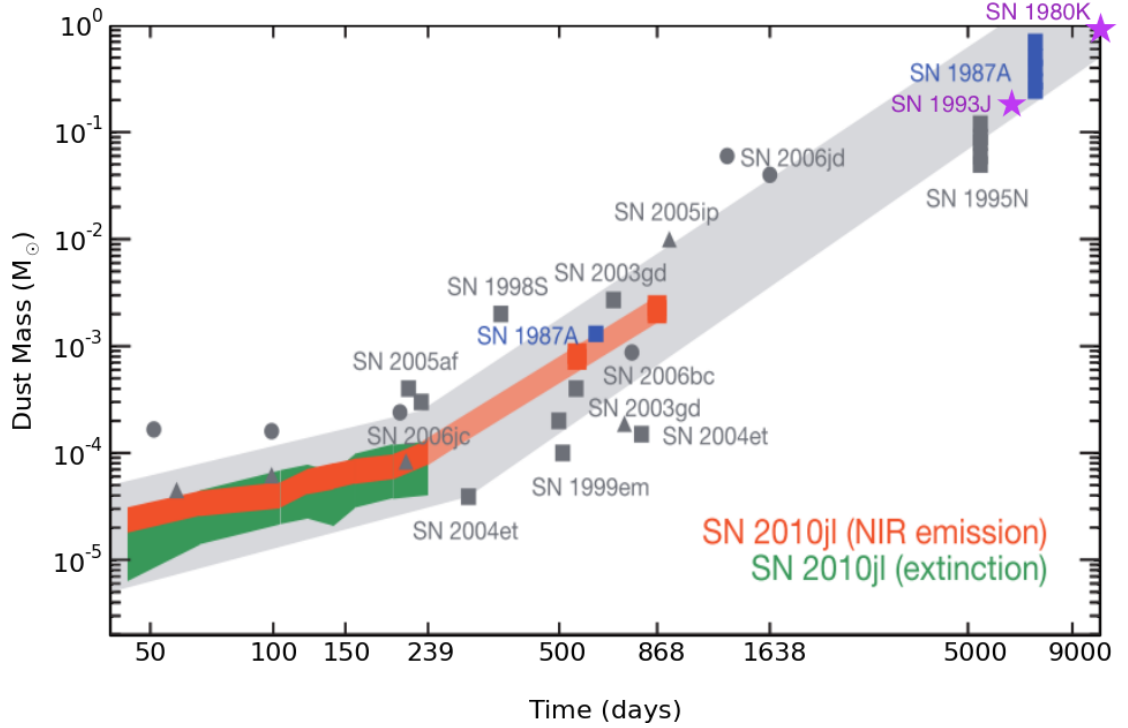


Figure 5.13. Dust formation rate in CCSNe as taken from the study of SN 2010jl by Gall et al. (2014). Over-plotted in purple stars are the dust masses derived from the amorphous carbon model of the [O I] doublet for SN 1980K and the silicate model of the [O III] doublet for SN 1993J showing the excellent agreement between their predicted rate and my results.

tatively using all of the available signatures discussed in Section 1.2.7. It is interesting to note that the dust masses inferred from polarised emission and from line profile asymmetries are in broad agreement but are not in agreement with dust masses inferred by fitting observations of dust emitting in the IR and sub-mm. Further line profile models of Cas A that adopt a more realistic and complex geometry and also include a more representative selection of species will hopefully constrain the dust masses more effectively.

5.4 Conclusions

It is notable that of the fairly small sample of CCSNe obtained by Milisavljevic et al. (2012) that were still visible at late times, a large number of them exhibited blue-shifted line profiles. This feature of the optical spectra of CCSNe at late times is most simply explained by the presence of dust in the ejecta. I have modelled oxygen and hydrogen lines in the optical region of the spectra of three SNRs and have found that in the majority of

cases, even for extremely old remnants, I can reproduce the profiles fairly well even with relatively simple models. Further modelling that allows for more complex geometries will likely allow for even better fits to be obtained. Regardless, it seems clear that the presence of newly-formed dust in the ejecta of these objects can account for the frequently seen blue-shifting of their line profiles.

My aim throughout the modelling of these three objects has been to determine the feasibility that it is dust causing the asymmetry observed in optical line profiles from CCSNe. It has also been to attempt to determine the expected order of magnitude of the dust masses that cause these characteristic dust-affected lines. Whilst the derived dust masses are highly dependent on clumping structures and dust composition, I find that large masses of dust are generally required to account for the degree of blue-shifting observed at late times.

In particular, I consider the dust formation rate in CCSNe considered by Gall et al. (2014). They bring together a number of dust mass estimates from the literature for a number of SNe based largely on SED fitting, predominantly at earlier times, and extrapolate a dust formation rate. I present this plot in Figure 5.13 and superimpose on it the dust masses that I derive for SN 1980K and SN 1993J. In both cases, I adopt the dust mass from the more realistic clumped models. For the purposes of considering how much dust may be formed in the ejecta of CCSNe, I plot the maximum dust mass I derive. For SN 1980K, this is $0.9M_{\odot}$ from the amorphous carbon model of the $[\text{O I}]\lambda\lambda 6300, 6363 \text{ \AA}$ doublet and for SN 1993J this is $0.18M_{\odot}$ from the silicate model of the $[\text{O III}]$ doublet. These values are very much in agreement with the dust formation rate suggested by Gall et al. (2014) and I note that even the other lower dust mass estimates that I derive are still mostly in reasonable agreement as well.

Cas A remains unique in being the only remnant of its age for which we have dust mass estimates. Establishing these estimates as accurately as possible is therefore extremely important. The masses I derive here are high, even for the most conservative case and would suggest that dust formation in Type IIb supernovae is just as effective as for other Type II SNe such as SN 1987A and SN 1980K. It is noted that there are strong similarities between the late-time spectra of SN 1993J and Cas A (Milisavljevic et al. 2012). Whilst the dust masses that I obtain for SN 1993J are perhaps a little lower than predicted by Gall et al. (2014), the models of Cas A might indicate that there is more yet to form.

Further modelling of these and other supernovae that exhibit characteristically blue-

shifted line profiles will hopefully shed more light on this issue.